Research Article

Design of Cr-Free Promoted Copper−Iron Oxide-Based High-Temperature Water−Gas Shift Catalysts

Ozgen Yalcin, Sagar Sourav, and Israel E. Wachs*

Cite This: ACS Catal. 2023, 13, 12681−12691

Read Online

ACCESS | Metrics & More | Article Recommendations

ABSTRACT: The effect of Ce addition to the Cr-free Al-promoted Cu−Fe oxide-based catalysts is investigated. Catalyst characterization (X-ray diffraction (XRD), in situ Raman spectroscopy, high-sensitivity low-energy ion scattering (HS-LEIS), Brunauer−Emmett−Teller (BET) analysis), CO-temperature-programmed reduction chemical probing, and steady-state WGS activity reveal that (i) in the absence of Al, Ce addition via coprecipitation has a detrimental effect on the catalytic activity related to the poor thermostability and formation of less active Ce−Cu−O NPs, (ii) the addition of Ce via coprecipitation also does not improve the performance of the CuAlFe catalyst because of the formation of a thick CeO_x overlayer on the active Cu−FeO_x interface, and (iii) impregnation of Ce onto the CuAlFe catalyst exhibits significant improvement in catalytic performance due to the formation of a highly active CeO_x−FeO_x−Cu interfacial area. In summary, Al does not surface-segregate and serves as a structural promoter, while Ce and Cu surface-segregate and act as functional promoters in Ce/CuAlFe mixed oxide catalysts.

KEYWORDS: high-temperature, water−gas shift, iron oxide-based catalysts, Cr-free catalysts, cerium oxide, aluminum oxide
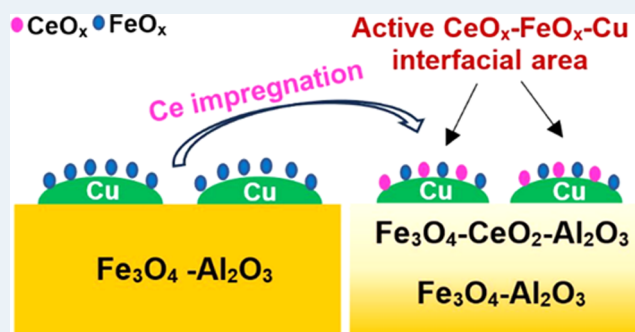
1. INTRODUCTION

The water−gas shift (WGS) reaction ($CO + H_2O \leftrightarrow CO_2 + H_2$) is an important step in the production of hydrogen from hydrocarbons and generally follows the steam reforming reaction for hydrogen enrichment and carbon monoxide elimination.[1−3] Industrially, the WGS reaction is performed in two steps: a high-temperature shift (HTS) (∼320−450 °C) reaction, followed by a low-temperature shift (LTS) (∼180−250 °C) reaction to achieve maximum equilibrium conversion for this equilibrated exothermic reaction.[4−8] Iron oxide-based catalysts containing 80−90 wt % Fe_2O_3, 8−10% Cr_2O_3, and the balance promoters such as copper oxide are used for the high-temperature water−gas shift (HT-WGS) reaction, and Cu-based catalysts (Cu−ZnO−Al_2O_3) are used for the low-temperature water−gas shift reaction.[5]

In situ/operando bulk and surface structural characterization of the HT-WGS iron−chromium oxide-based catalysts revealed the molecular structure and nature of the active site during the HT-WGS reaction. In the freshly calcined chromium−iron oxide-based HT-WGS catalysts, prepared by coprecipitation of iron and chromium oxide precursors, followed by calcination, iron oxide is present as the bulk hematite (α-Fe_2O_3 or γ-Fe_2O_3) phase.[5] *In situ* Raman and high-sensitivity low-energy ion scattering (HS-LEIS) measurements reveal that Cr^{6+} oxide is mostly present on the surface of the bulk Fe_2O_3 phase in the fresh catalyst.[9,10] After activation

of the catalyst under HT-WGS reaction conditions, the bulk Fe_2O_3 phase transforms to the bulk Fe_3O_4 (magnetite) phase, which is the bulk catalytic active phase of iron oxide during the HT-WGS reaction.[7] During the HT-WGS reaction, the surface Cr^{6+} oxide also reduces to Cr^{3+} oxide and forms a solid solution with the Fe_3O_4 lattice ($Fe_{3−x}Cr_xO_4$).[11−13] The $Fe_{3−x}Cr_xO_4$ solid solution also stabilizes the iron oxide phase from becoming reduced to metallic Fe^0, which can form undesired hydrocarbons, showing that chromium oxide serves as a textural promoter.[9,10]

The chromium−iron oxide-based HT-WGS catalysts possess several wt % Cr^{6+} when exposed to air in the fresh and spent catalysts, which is problematic since hexavalent Cr^{6+} is a carcinogen that threatens human health and the environment.[8,14] Consequently, rigorous investigations have been performed to find a suitable nontoxic replacement of chromium exhibiting equivalent or better HT-WGS catalytic performance. Some of the elements investigated as potential replacements for Cr in the iron oxide-based HT-WGS catalysts

are Al, Zn, Ca, Ni, Co, Ge, Mg, Ti, Si, Mo, Ce, Zr, and Nb.[8,15−28]

Many of these studies use copper oxide as a chemical promoter for iron oxide-based HT-WGS catalysts. Recent *in situ* characterization studies show that in the fresh catalyst, Cu is present as Cu^{2+} oxide in the lattice of the Fe_2O_3 phase. After activation of the catalyst under the HT-WGS reaction environment, Cu oxide reduces and segregates as metallic copper nanoparticles on the surface of the Fe_3O_4 phase (*in situ* X-ray absorption fine structure (XAFS), near-ambient-pressure X-ray photoelectron spectroscopy (NAP-XPS), X-ray absorption near-edge spectroscopy (XANES)).[10,29−31] Interestingly, a fraction of the metallic copper nanoparticle surface was found to have been covered by an FeO_x overlayer (HS-LEIS and transmission electron microscopy (TEM)).[10] The copper promotion is realized by the introduction of new catalytic active sites, present as an interfacial area of the FeO_x overlayers and Cu nanoparticles that increases the activity of HT-WGS. It was observed that the turnover frequency (TOF) value of chromium−iron oxide catalyst (1.2×10^{-3} s^{-1}) increased by ~3× (3.5×10^{-3} s^{-1}) upon the addition of copper.[32]

Recent findings from Cr-free iron oxide-based HT-WGS studies[15,21,22,33−38] confirm that aluminum is a very promising substitute for the Cr promoter. The Al promoter exhibits comparable structural stability, thermostability, and catalytic activity as that of the Cr-promoted HT-WGS catalysts.[19] Cerium, a rare earth metal, is another promising promoter[33,39−43] due to its high oxygen storage capability and excellent redox ability to change oxidation states between Ce^{4+} ↔ Ce^{3+}.[44] The combination of the Ce−Al[33] and Ce−Zr[39] promoters was found to enhance the thermal stability of iron oxide-based catalysts, even after several HT-WGS reaction cycles. Ceria promotion has also been suggested to have an electronic effect on catalytic activity.[40] Unfortunately, these studies lacked critical direct *in situ* spectroscopic details about the dynamics of the catalyst structure to determine the actual promotion mechanism of Ce oxide, which is the motivation for the current study.

The objective of the current work is to understand the combined promotional effect of ceria and alumina promoters on Cr-free copper−iron oxide-based HT-WGS catalysts. For this purpose, coprecipitation and incipient-wetness impregnation of the Ce oxide promoter in copper−aluminum−iron oxide catalysts with varying Ce and Al loadings were done. The Brunauer−Emmett−Teller (BET) surface areas of the fresh and activated catalysts were measured *in situ*, without exposing the pyrophoric catalyst to the atmosphere. The bulk structure of the catalyst was determined with X-ray diffraction (XRD). *In situ* Raman spectroscopy measurements provided information about the bulk as well as surface structure of various metal oxides present in the catalysts under different environmental conditions. Additionally, the topmost surface layer of the catalysts was characterized with HS-LEIS spectroscopy. The catalyst reducibility was chemically probed by CO-temperature-programmed reduction (TPR) experiments, and the catalytic performance of various catalysts was compared via the steady-state HT-WGS reaction. The current findings offer an insight into the design of chromium-free iron oxide-based HT-WGS catalysts.

2. EXPERIMENTAL SECTION

2.1. Catalyst Synthesis.
Cerium-, aluminum-, and copper-doped iron oxide catalysts were prepared by using cerium(III)

nitrate hexahydrate ($Ce(NO_3)_3 \cdot 6H_2O$, Alfa Aesar), aluminum nitrate nonahydrate ($AlN_3O_9 \cdot 9H_2O$, Sigma-Aldrich 99.99% trace metal basis), copper(II) nitrate hemi(pentahydrate) ($CuN_2O_6 \cdot 2.5H_2O$, Aldrich 99.99% trace metal basis), and iron(III) nitrate nonahydrate ($FeN_3O_9 \cdot 9H_2O$, Sigma-Aldrich 99.99% trace metal basis) precursors. Two different methods were followed for incorporation of the Ce promoter.

In the coprecipitation method, calculated amounts of all of the metal oxide precursors were dissolved in 100 mL of distilled water and mixed well. To this solution, ammonium hydroxide solution (30%, m/v) was added dropwise under constant stirring at room temperature until the pH reached 8.5. At this point, the formation of a dark brown precipitate was observed and was further aged for 24 h at room temperature, followed by filtration. The filtered precipitate was then put in a temperature-programmable oven. It was dried at 80 °C for 12 h and finally calcined at 400 °C for 4 h in a static air environment. These catalysts contain 8 wt % Ce and/or Al promoters, 3 wt % Cu promoter, and 89 wt % iron, in the oxidized form. The catalysts synthesized using the coprecipitation method are denoted as follows: 3Cu8AlFe, 3Cu8CeFe, and 3Cu5Al3CeFe.

The Ce promoter was added via incipient-wetness impregnation to the copper−aluminum−iron oxide catalyst, prepared by the coprecipitation method (3Cu8AlFe). The calculated amount of Ce oxide precursor aqueous solution was added dropwise. The impregnated sample was then dried for 24 h at room temperature, followed by additional drying at 80 °C for 12 h and finally calcined at 400 °C for 4 h, under static air environment. These catalysts are denoted by 3Ce/3Cu8AlFe and 5Ce/3Cu8AlFe. In all preparation steps, the final calcined catalysts were always ground to make a fine powder.

2.2. BET Surface Area Measurement.
The surface area values of both fresh and WGS reaction mixture-treated catalysts were measured by a 3-point flow BET method in an Altamira Instruments system (AMI-200) equipped with a TCD detector. After preconditioning of the catalysts and prior to the BET measurements, all samples were degassed under He flow at ~150 °C. The N_2 adsorption/desorption amounts were measured at three different partial pressures (P/P_0 = 0.14, 0.22, and 0.30) for the calculation of surface area values. The fresh catalysts were always dehydrated at 400 °C, under flowing 10% O_2/Ar (Praxair, for 1 h), prior to BET measurements. For catalyst activation under HT-WGS reaction conditions, 10% CO/Ar (Praxair, 10 mL/min) and He (Airgas, UHP certified gas, 30 mL/min) gas mixture was passed through a water saturator at room temperature to maintain a CO/H_2O ratio ~1. The catalysts were activated at 330 °C for 1 h and 500 °C for 2 and 5 h. Any residual gases were flushed with He after the HT-WGS reaction. The surface areas of the activated catalysts were measured without exposing the catalysts to the ambient atmosphere (*in situ* BET measurements).

2.3. X-ray Diffraction (XRD) Spectroscopy.
Powder X-ray diffraction patterns of fresh calcined catalysts were measured by the Panalytical Empyrean X-ray Diffraction Unit under ambient conditions. The Cu attenuator mask was utilized for alignment. Full scans between 20 and 80° (2Θ) at a rate of 5°/min were utilized. Additionally, the Fe_2O_3 (110) peak in the range of 34.5−36.5° was scanned with a rate of 1°/min.

2.4. *In Situ* Raman Spectroscopy.
The Raman spectroscopic studies were performed with a Horiba-Jobin

Table 1. BET Surface Area of Various Cu−Al−Ce−Fe Oxide Catalysts after Dehydration: 10% O$_2$/Ar at 400 °C for 1 h and WGS Reaction: 10% CO/Ar (10 mL/min), He (30 mL/min), and Water Vapor (H$_2$O/CO ∼1) at 330 (for 1 h) and 500 °C (for 2 and 5 h)

		BET surface area (m^2/g)			
sample	composition (wt %)	fresh	330 °C, 1 h	500 °C, 2 h	500 °C, 5 h
3Cu8AlFe[a]	3% CuO − 8% Al$_2$O$_3$ − 89% Fe$_2$O$_3$	86	44	25	23
3Cu8CeFe[a]	3% CuO − 8% CeO$_2$ − 89% Fe$_2$O$_3$	74	34	23	20
3Cu5Al3CeFe[a]	3% CuO − 5% Al$_2$O$_3$ − 3% CeO$_2$ − 89% Fe$_2$O$_3$	97	43	27	25
3Ce/3Cu8AlFe[b]	3% CeO$_2$/(3% CuO − 8% Al$_2$O$_3$ − 89% Fe$_2$O$_3$)	79	50	29	28
5Ce/3Cu8AlFe[b]	5% CeO$_2$/(3% CuO − 8% Al$_2$O$_3$ − 89% Fe$_2$O$_3$)	73	48	28	26

[a]Coprecipitated. [b]Coprecipitation, followed by impregnation of Ce.

Yvon LabRam High-Resolution instrument equipped with a confocal microscope (50× long working distance objective, Olympus BX-30-LWD). A laser excitation of 442 nm (generated by a He−Cd laser, 110 mW maximum power) and single-stage monochromator with 900 grooves/mm grating were utilized for spectra collection. The scattered light from the sample was passed through the monochromator grating and collected with a visible sensitive liquid N$_2$-cooled CCD detector (Horiba-Jobin Yvon CCD-3000 V). Catalysts were placed in a high-temperature reactor cell (Linkam CCR1000) with a temperature controller (Linkam TMS94). Spectra of the dehydrated samples were collected after removal of any possible organic impurities and adsorbed moisture by flowing of 10% O$_2$/Ar (Praxair) with 30 mL/min flow rate at 400 °C for 1 h. For the collection of *in situ* spectra of the activated catalysts during the reverse-WGS (RWGS) reaction, the catalysts were further treated with a mixture of 30 mL/min 5%CO$_2$/Ar (GTS-WELCO) and a 15 mL/min 10%H$_2$/Ar (Airgas, UHP certified gas) mixture at 400 °C for 1 h.

2.5. High-Sensitivity Low-Energy Ion Scattering (HS-LEIS) Spectroscopy. The HS-LEIS surface analysis of the catalysts was performed in an ION-TOF Qtac^{100} spectrometer. Powder catalyst samples were compressed in a sample holder for heat treatments within the HS-LEIS spectrometer. The design of the HS-LEIS instrument allows one to directly transfer the sample from the pretreatment chamber to the analysis chamber without exposing to the ambient atmosphere. The fresh catalyst samples were dehydrated in a ∼10 mbar 10% O$_2$/Ar static gas environment at 400 °C for 1 h. The RWGS reaction mixture-activated catalysts were conditioned in the ∼10 mbar static gas mixture environment of CO$_2$ + H$_2$ (CO$_2$/H$_2$ ratio ∼1) at 400 °C for 1 h. After the desired pretreatment, the topmost surface of the catalyst was analyzed using 3 keV He$^+$ (for lighter atomic weight elements like O and Al) and 5 keV Ne$^+$ (for heavier elements like Fe, Cu, and Ce) ion probes. Further, to gain information about the composition of subsurface layers, the topmost layer was sputtered with 0.5 keV Ar$^+$ ions allowing for depth profiling. Charge neutralization was invoked during spectral acquisition as well as sputtering steps. The probes employed were 3 keV He$^+$ (1 × 10^{14} ions/cm^2·cycle) and 5 keV Ne$^+$ (1 × 10^{14} ions/cm^2·cycle), 1.5 × 1.5 mm^2. For sputtering, 0.5 keV Ar$^+$ (1.5 × 10^{14} ions/cm^2·cycle, 2.0 × 2.0 mm^2) was applied. A dose of 1 × 10^{15} ions/cm^2 corresponds to removal of approximately one atomic layer from the catalyst surface.[45]

2.6. CO-Temperature-Programmed Reduction (TPR). The CO-TPR experiments were performed using an Altamira Instruments system (AMI-200) equipped with a Dycor Dymaxion DME100MS online quadrupole mass spectrometer. Dehydrated catalysts (under flowing 10% O$_2$/Ar, Praxair, at

350 °C for 1 h) were activated via the HT-WGS reaction (10 mL/min 10% CO/Ar (Praxair), 30 mL/min He (Airgas, UHP certified gas), flow through bubbler at room temperature) at 350 °C for 90 min. After the activation process, the reactor was flushed by He and cooled down to 80 °C. The CO-TPR experiments were then carried out by ramping up the temperature under 10% CO/Ar (Praxair) at a rate of 10 °C/min with simultaneous online gas analysis by a mass spectrometer. The resulting CO$_2$/CO-TPR spectra were normalized by the MS signal for Ar that was used as the internal standard.

2.7. Steady-State HT-WGS Reaction. The steady-state forward water−gas shift reaction activity measurements were carried out by using an Altamira AMI-200 instrument equipped with a Dycor Dymaxion DME100MS online quadrupole mass spectrometer. Approximately 10 mg of the powder catalyst was loaded into a U-type quartz tube and held in place with quartz wool. First, 10% O$_2$/Ar (Praxair) was passed with a flow rate of 40 mL/min at 400 °C for 1 h to remove any possible adsorbed organics. Then, the system was flushed with He for 10 min. Afterward, the reaction mixture was introduced (10% CO/Ar (Praxair, 10 mL/min), He (Airgas, UHP certified gas, 30 mL/min), and water vapor introduced by flowing the gas through a water bubbler at room temperature). The total flow rate was 40 mL/min for approximately 10 mg catalyst. The GHSV equals 240,000 mL/h·gcat. This high GHSV maintains low conversion with minimal transport limitations.[46] The HT-WGS reaction was performed at different temperatures (330, 350, 370 °C) for 90 min to ensure steady-state conditions. The following *m/z* values were recorded during the experiment: H$_2$, *m/z* = 2; H$_2$O, *m/z* = 18; CO (corrected for CO$_2$ cracking), *m/z* = 28; CO$_2$, *m/z* = 44; and Ar, *m/z* = 40. Ar was used as an internal standard.

3. RESULTS

3.1. BET Surface Area. The BET surface area values of freshly calcined and activated catalyst samples exposed to the WGS reaction are listed in Table 1. To compare the thermostability of the catalyst samples, the HT-WGS reaction treatment was conducted at multiple temperatures (330 °C for mild reaction conditions and 500 °C for more rigorous reaction conditions) and durations (1−5 h).

3.1.1. Fresh Catalysts. The coprecipitated 3Cu8AlFe catalyst has a BET surface area of 86 m^2/g. Replacement of Al oxide with equivalent weight loading of a Ce oxide (3Cu8CeFe) catalyst results in a decrease in the surface area to 74 m^2/g. The mixture of coprecipitated Al and Ce oxides, with equivalent total promoter loading of 8 wt % (3Cu5Al3CeFe),
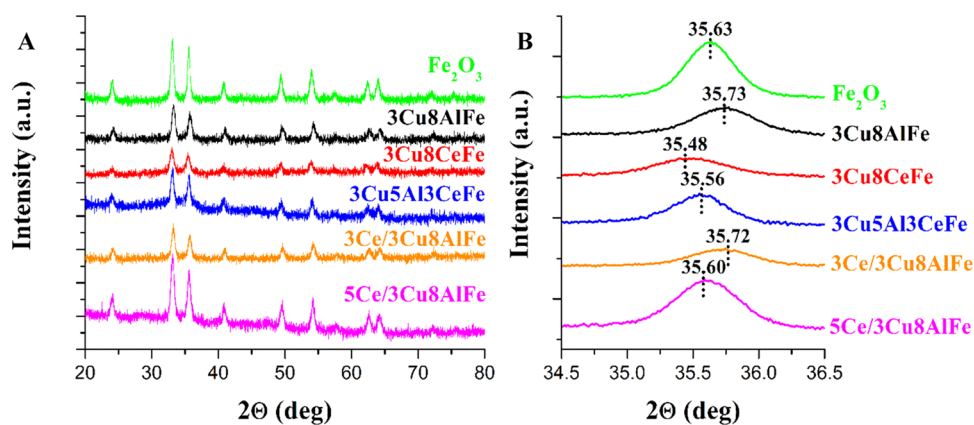
Figure 1. XRD diffractograms of fresh calcined catalysts collected under ambient conditions as a function of 2Θ (A) full scan and (B) the Fe_2O_3 (110) peak region.
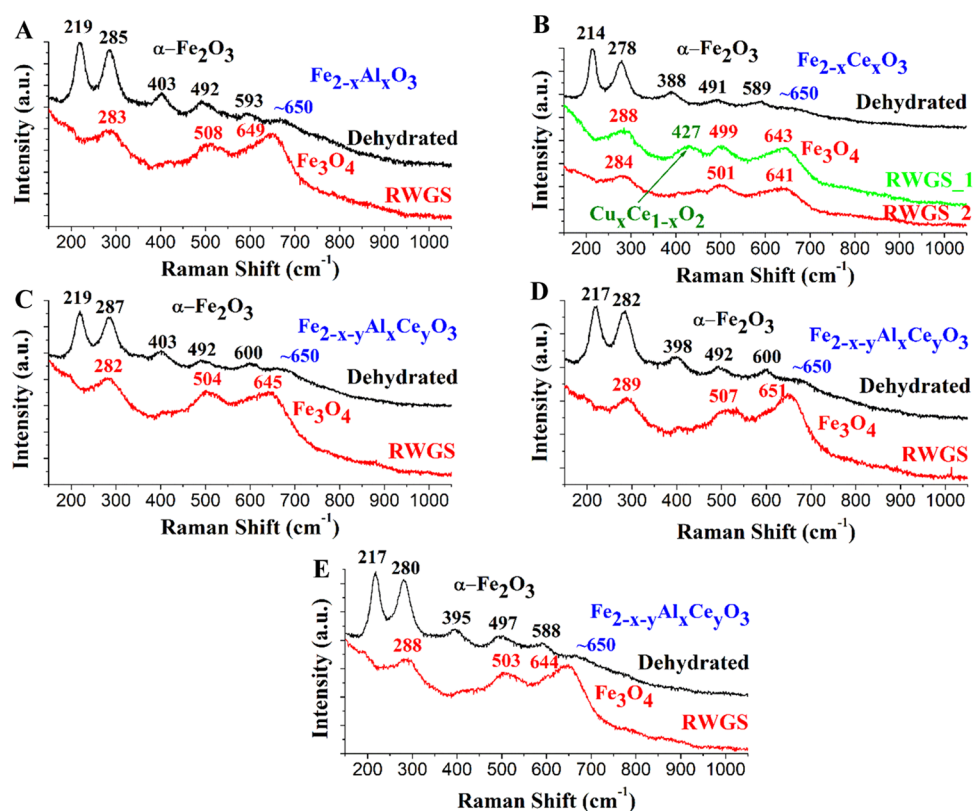

Figure 2. *In situ* Raman spectra of (A) 3Cu8AlFe, (B) 3Cu8CeFe, (C) 3Ce/3Cu8AlFe, (D) 5Ce/3Cu8AlFe, and (E) 3Cu5Al3CeFe catalysts under dehydrated (10% O_2/Ar) and RWGS reaction conditions (30 mL/min 5%CO_2/Ar and 15 mL/min 10%H_2/Ar) at 400 °C. RWGS_1 and RWGS_2 denote spectra collection from two different points on the catalyst surface.

however, increases the BET surface area of the catalyst to 97 m^2/g. In contrast, impregnation of the 3 and 5% Ce onto the coprecipitated calcined 3Cu8AlFe catalysts showed an opposite trend in BET surface area values with the surface areas decreasing to 79 and 73 m^2/g, respectively. Overall, the initial BET values only modestly varied (73−97 m^2/g) with the coprecipitated catalysts possessing slightly higher BET values.

3.1.2. HT-WGS-Activated Catalysts. After activation of the catalyst samples under the HT-WGS reaction conditions, the surface area of all of the samples decreased significantly (Table 1). Even after mild activation (330 °C, 1 h treatment), a 35−55% decrease in the surface area of the catalyst samples occurred. Under the milder HT-WGS conditions (330 °C, 1 h

treatment), the 3Cu8CeFe catalyst exhibited the lowest BET surface area of 34 m^2/g, and all of the other catalysts possessed surface area values in a close range (44−50 m^2/g) with the 3Ce/3Cu8AlFe catalyst having the highest surface area. After the harsher treatment of the catalyst samples (at 500 °C for 5 h), all of the catalysts showed a significant decrease of ∼60−75% in the surface area compared to their respective fresh catalysts. Although the surface area values are close to each other, the 3Cu8CeFe exhibits slightly poorer thermostability and the catalysts that were impregnated with ceria or coimpregnated with Ce and Al exhibited slightly better thermostability. The more harshly activated catalysts, however,
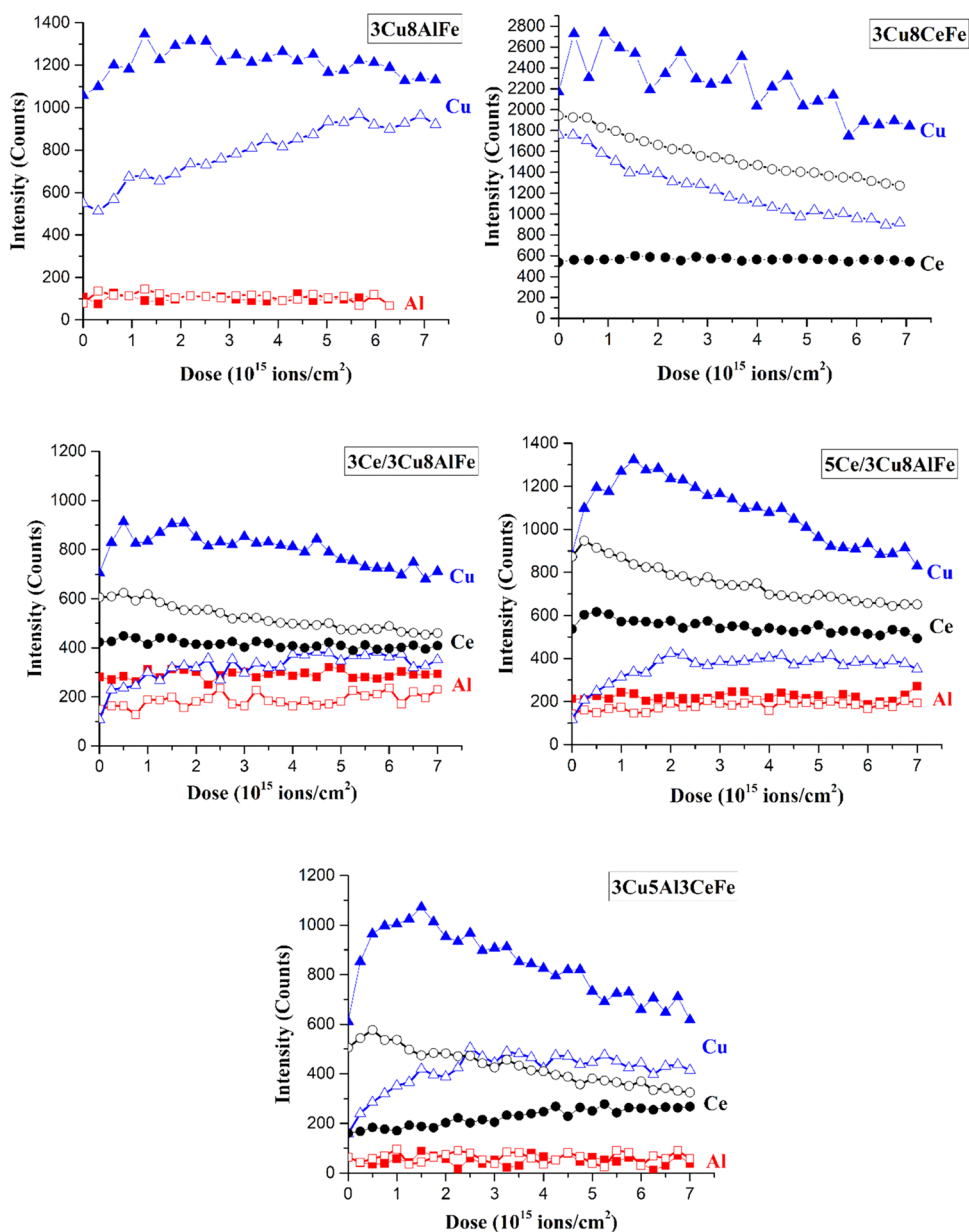
Figure 3. HS-LEIS depth profile of O_2 calcined (solid symbols) and RWGS reaction ($CO_2 + H_2$) activated (open symbols) catalysts after pretreatments. The He^+ ion is the probe for Al and the Ne^+ ion is the probe for Ce and Cu (Cu: blue rectangle; Ce: black sphere; Al: red square).

possess very similar BET surface areas that are independent of the composition and synthesis method.

3.2. XRD. The XRD diffractograms of the freshly calcined catalysts under ambient conditions are presented as full scans, and the main $Fe_2O_3(110)$ peaks are shown in Figure 1. The bulk phase of the initial promoted iron oxide catalysts is crystalline α-Fe_2O_3 (hematite).[47] The intensity of the $Fe_2O_3(110)$ peak decreases with Al and Ce addition, most probably from a decrease in particle size and/or greater disorder. The X-ray diffraction patterns of all catalysts do not show any observable distinct nanoparticles of crystalline Al_2O_3,[48] CeO_2,[49] CuO_x, or any compounds between Cu−Ce−Al−Fe oxides. This observation suggests that these NPs are either absent or are too small (<3 nm) to be detected by XRD. The (110) hematite peak can be used to examine for possible solid solutions of the promoters and the iron oxide catalyst. The slight shift of (110) hematite peak in the XRD

indicated solid solution formation between Cr oxide and Fe_2O_3 in excellent agreement with prior studies.[10] The slight, yet opposite, shift of the $Fe_2O_3(110)$ peak for both 3Cu8AlFe and 3Cu8CeFe catalysts, compared to the unpromoted Fe_2O_3 catalyst, indicates that a solid solution is formed between Al oxide and Fe_2O_3 as well as Ce oxide and Fe_2O_3, respectively. This is consistent with the smaller ionic radii of Al^{3+} (53.5 pm)[50] than the ionic radius of Fe^{3+} (64.5 pm)[50] and the larger ionic radii of Ce^{4+} (87 pm)[50]/Ce^{3+} (101 pm)[50] than the ionic radius of Fe^{3+} (64.5 pm).[50] Incorporation of ceria into the alumina-containing catalysts has different effects. Coprecipitation of alumina and ceria promoters (3Cu5Al3CeFe catalyst) shows the dominant effect of larger ionic radii of the cerium ion as the 2θ position of the main (110) peak slightly decreases compared to the unpromoted Fe_2O_3 phase. On the other hand, the amount of ceria loading determines the 2θ position of the main (110) peak of the Fe_2O_3 phase of ceria-impregnated

3Cu8AlFe catalysts. For the impregnated 3Ce/3Cu8AlFe catalyst, the Fe_2O_3 110 peak remains the same as that of the 3Cu8AlFe catalyst. This suggests that 3 wt % loading of Ce oxide by impregnation has a very limited effect on the solid solution of Al with the Fe_2O_3 phase. An increase in the ceria loading to 5 wt % reflects the effect of Ce incorporation into the Al−Fe_2O_3 solid solution phase and is indicated by the shift of the $Fe_2O_3(110)$ peak compared to the 3Cu8AlFe catalyst. Although the XRD spectra were not collected for the WGS-activated catalysts, previous *in situ* XRD studies showed that the bulk iron oxide Fe_2O_3 (hematite) phase transforms to the Fe_3O_4 (magnetite) phase (see the Section 3.3 for confirmation).[19] Although the promoters formed solid solutions with the Fe oxide phases, they did not affect the bulk structure of the Fe oxide phase.

3.3. *In Situ* Raman Spectroscopy. The *in situ* Raman spectra of the calcined catalysts are presented in Figure 2. The Raman spectra of all of the dehydrated freshly calcined catalysts exhibit the characteristic bands of the bulk α-Fe_2O_3 phase (hematite: 226, 245, 292, 411, 497, 612 cm^{-1}).[51] The weak and broad new band at 620−700 cm^{-1} has been attributed to crystal disorder caused by the solid solution of $Fe_{2-x}M_xO_3$ (M: Al and/or Ce) with small crystalline dimensions.[52]

Under the RWGS reaction conditions, the bulk α-Fe_2O_3 (hematite) phase reduces to the bulk Fe_3O_4 (magnetite) phase (306, 538, 668 cm^{-1}).[53] This is in agreement with literature reports that the Fe_3O_4 phase is the dominant bulk phase of iron oxide under HT-WGS reaction conditions.[7] No additional NPs from the Ce, Cu, and Al are observed for any of the Al-containing catalysts. A new broad Raman band at ∼427 cm^{-1}, however, is observed for the 3Cu8CeFe catalyst and can be assigned to the mixed oxide phase of Ce with Cu (Ce−Cu−O solid solution).[54] The spectra of the 3Cu8CeFe catalyst collected from different spots, however, indicate that the Cu−Ce−O mixed oxide phase, formed during the RWGS reaction, does not uniformly cover the catalyst surface. This Raman band, however, was not detected in the Raman spectra of any of the Cu−Ce−Al−Fe oxide catalysts. The *in situ* Raman spectra confirm that the same bulk Fe oxide phases are present among all of the freshly calcined catalysts and among all of the activated catalysts. The presence of a bulk $Cu_xCe_{1-x}O_2$ mixed oxide phase was also detected for the activated 3Cu8CeFe catalyst.

3.4. High-Sensitivity Low-Energy Ion Scattering (HS-LEIS) Spectroscopy. Elemental compositional analysis of the outermost surface layer and subsequent subsurface layers by depth profiling of the synthesized catalysts, after dehydration and activation under RWGS reaction conditions, were measured with HS-LEIS and are presented in Figure 3. The Fe signal is not shown in any of the HS-LEIS spectra because previous investigations showed a significant increase in the Fe signal intensity due to preferential sputtering of oxygen from iron oxides.[55,56] The intensity of the Al signal is relatively lower than the intensity of the Cu and Ce signals because the Al signals were collected with the lighter He$^+$ ions and Cu/Ce signals were collected with the heavier Ne$^+$ ions.

3.4.1. 3Cu8AlFe Catalyst. In the dehydrated freshly calcined catalyst (see Figure 3 solid symbols), the intensity of the Al and Cu signals is relatively the same on the outermost surface layer and throughout the subsurface region of the catalyst, indicating that Al and Cu are uniformly distributed in the outermost surface layers of this dehydrated catalyst. Upon catalyst activation in the RWGS reaction environment, the intensity of the Al signal remained constant and the intensity of the Cu signal increased in the outermost surface layer (see Figure 3 open symbols). After activation of the catalyst, the intensity of the Al signal remains constant, suggesting uniform distribution of Al with depth, but the intensity of the Cu signal monotonically increased with depth profiling, reflecting the covering of the Cu nanoparticles most likely with an FeO_x overlayer.[19]

3.4.2. 3Cu8CeFe Catalyst. For the dehydrated freshly calcined catalyst (see Figure 3 solid symbols), the intensity of the Ce signal remains relatively the same from the outermost surface layer to the subsurface layers reflecting its uniform distribution with depth. The corresponding intensity from Cu mildly decreases with sputtering depth, suggesting that Cu is slightly surface-enriched. Upon catalyst activation under RWGS (see Figure 3 open symbols), the intensity of the Cu signal decreased and the intensity of the Ce signal slightly decreased at the outermost surface layer. Furthermore, the intensity of both Cu and Ce signals decreases with catalyst activation, reflecting surface enrichment of both Cu and Ce.

3.4.3. 3Ce/3Cu8AlFe Catalyst. For the dehydrated catalyst (see Figure 3 solid symbols), the intensity of the Al and Ce signals remains constant from the outermost surface layer and subsurface layers of the catalyst. The Cu intensity, however, decreases slightly with depth profiling. After activation under RWGS (see Figure 3 open symbols), the intensity at the outermost surface layer for Al slightly increases, Cu significantly increases, and Ce remains constant. During depth profiling, the intensity of the Al signal is constant, the Ce signal slightly decreases and Cu signal increases up to 1−2 atomic layers and stays nearly constant after that, reflecting the surface enrichment of Ce and surface depletion of Cu. Furthermore, the Ce oxide NPs decorating the Cu surface are ∼3−4 nm in size.

3.4.4. 5Ce/3Cu8AlFe Catalyst. For the dehydrated catalyst (see Figure 3 solid symbols), during sputtering, the intensities of the Al and Ce signals are relatively constant, indicating the uniform concentration of Al and Ce from the outermost surface layer to the subsurface layers. The intensity of the Cu signal, however, initially increases and then decreases reflecting the concentration of Cu peaking in the subsurface region. After RWGS treatment of the catalyst (see Figure 3 open symbols), the intensity at the outermost surface layer of Al does not change, Ce increased, and Cu decreased. With depth profiling, the intensity of Al remained the same, Cu increased, and Ce monotonically decreased. The Cu signal intensity first increased until ∼2 atomic layers and then remained constant. These trends suggest that the Al makes a solid solution with the Fe_3O_4 phase, and Cu NPs present on the catalyst surface are decorated by ∼0.5 nm size Ce oxide NPs.

3.4.5. 3Cu5Al3CeFe Catalyst. In the dehydrated freshly calcined catalyst, the Al signal has the same intensity for the outermost surface layer and subsurface region. In contrast, the intensity from Ce increases slightly with depth profiling. The signal intensity from Cu first increases up to about a monolayer and then decreases with depth profiling. After treatment of the catalyst in the RWGS environment, no change in the Al signal intensity is observed between the outermost surface layer and the subsurface of the catalyst. The Ce signal intensity is observed to decrease monotonically with depth profiling. Finally, the signal from Cu increased for the initial 2−3 atomic layers and then remained nearly constant. These trends suggest

the formation of a thicker Ce oxide overlayer on the Cu NP surface.

3.5. CO-TPR. The reducibility of the WGS reaction-activated catalysts was examined with CO-TPR since CO oxidation represents a key reduction step in the WGS reaction. The normalized CO_2 MS signals, obtained by using Ar as an internal standard, as a function of the catalyst bed temperature, are presented in Figure 4. The formation of CO_2 at the lower
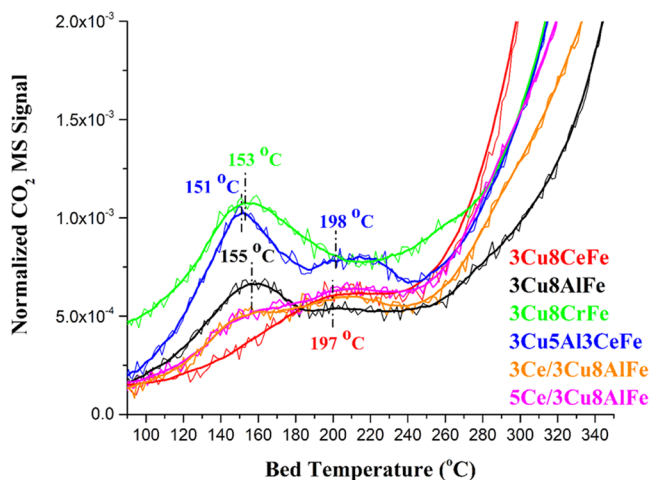

Figure 4. CO-TPR spectra of catalysts activated under the WGS reaction conditions at 350 °C.

temperatures is assigned to the removal of oxygen from the surface region of the catalyst, and the CO_2 formed at higher temperatures is associated with the reaction of CO with oxygen from the bulk lattice.[10] The strong consumption of CO starts at ~260 °C due to the deep reduction of the bulk Fe oxide phase.

The 3Cu8AlFe and 3Cu8CeFe catalysts possess only one low-temperature CO_2/CO-TPR reduction peak at 155 and 197 °C, respectively. For reference, the 3Cu8CrFe catalyst exhibits only one low-temperature CO_2/CO-TPR reduction peak at 153 °C that is similar to that of the 3Cu8AlFe catalyst. The 3Cu5Al3CeFe mixed oxide catalyst, however, has two distinct low-temperature CO_2/CO-TPR reduction peaks at 151 and 198 °C. The ceria-impregnated xCe/3Cu8AlFe catalysts show two CO_2/CO-TPR reduction peaks in the similar temperature ranges as that of the 3Cu5Al3CeFe catalyst. This observation suggests that the origin of the CO_2/CO-TPR reduction peak at ~150−155 °C is related to the effect of Al, while the 195−200 °C CO_2/CO-TPR reduction peak is associated with the Ce promoter.

The areas under the low-temperature CO_2/CO-TPR curves were used to quantify the number of redox catalytic active sites (Ns) present in each catalyst, and the values are listed in Table 2. It is assumed that the overall catalytic activity is dominated by the active sites available at the lowest temperature for CO oxidation.[20] An Al-free 3Cu8CeFe catalyst has the highest Ns value. While coprecipitation of the Ce promoter in the Cu−Al−Fe catalyst slightly increases the Ns value, the Ns value of the 3Cu8AlFe catalyst is slightly decreased by the impregnation of the Ce promoter. The numbers of reducible active sites of the two ceria-impregnated catalysts are similar but somewhat lower than those of the other catalysts. Impregnation of cerium oxide apparently decreases the number of the

Table 2. Number of Active Sites (Ns), Catalytic Activities Based on the CO Consumption Rate [$(10^{-6}$ mol/s/g) (10% CO/Ar (10 mL/min), He (30 mL/min), and Water Vapor (H_2O/CO ~ 1)) (T = 330 °C)], Turnover Frequencies (TOFs), and Activation Energies of Cu−Al−Ce−Fe Oxide Catalysts

catalyst	catalytic activity (10^{-6} mol/s·g)	number of active sites from CO-TPR (Ns) (10^{-3} mol/g)	TOF (10^{-3} s^{-1})	activation energy (E_a) (kJ/mol)
3Cu8AlFe	4.1 ± 0.2	0.87	4.7	56
3Cu8CeFe	3.7 ± 0.2	1.05	3.5	63
3Cu5Al3CeFe	4.3 ± 0.3	0.93	4.6	56
3Ce/3Cu8AlFe	6.5 ± 0.4	0.80	8.1	41
5Ce/3Cu8AlFe	5.2 ± 0.3	0.79	6.6	41

catalytic active sites, whereas the cerium-coprecipitated catalysts have a higher number of active sites.

3.6. Steady-State WGS Reaction. The steady-state catalytic activity values of the catalysts (based on the CO conversion) at 330 °C are presented in Table 2. Although the catalytic activity of 3Cu8CeFe is lower than the activity of 3Cu8AlFe, replacement of some amount of alumina with ceria by the coprecipitation method (3Cu5Al3CeFe catalyst) increases the activity. The main effect of ceria promotion is seen on the catalytic activity of the catalysts that are prepared by impregnation of ceria into 3Cu8AlFe catalysts. Impregnation of 3 wt % ceria dramatically increases the activity of the 3Cu8AlFe catalyst. Higher loadings of impregnated ceria result in a decrease in activity, which is still higher than the activity of the 3Cu8AlFe catalyst. The 3Ce/3Cu8AlFe catalyst is the most active, and the 3Cu8CeFe catalyst is least active. The steady-state activity follows the order 3Ce/3Cu8AlFe > 5Ce/3Cu8AlFe > 3Cu5Al3CeFe ~ 3Cu8AlFe > 3Cu8CeFe.

The TOF values (Table 2) were calculated by dividing the values of the steady-state catalytic activity by the number of participating surface redox oxygen atoms. The TOF values vary from 3.5×10^{-3} to 8.1×10^{-3} s^{-1} with the order of 3Ce/3Cu8AlFe > 5Ce/3Cu8AlFe > 3Cu5Al3CeFe ~ 3Cu8AlFe > 3Cu8CeFe, which is the same as the steady-state catalytic activity trend.

Differences in the catalytic activities are further examined by generating Arrhenius plots, shown in Figure 5. The
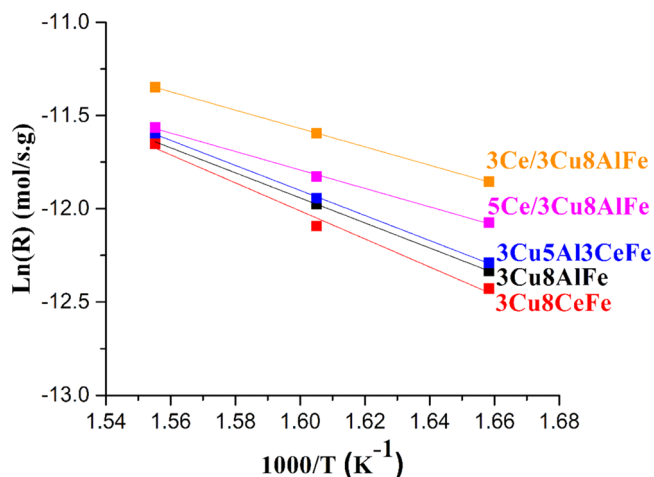

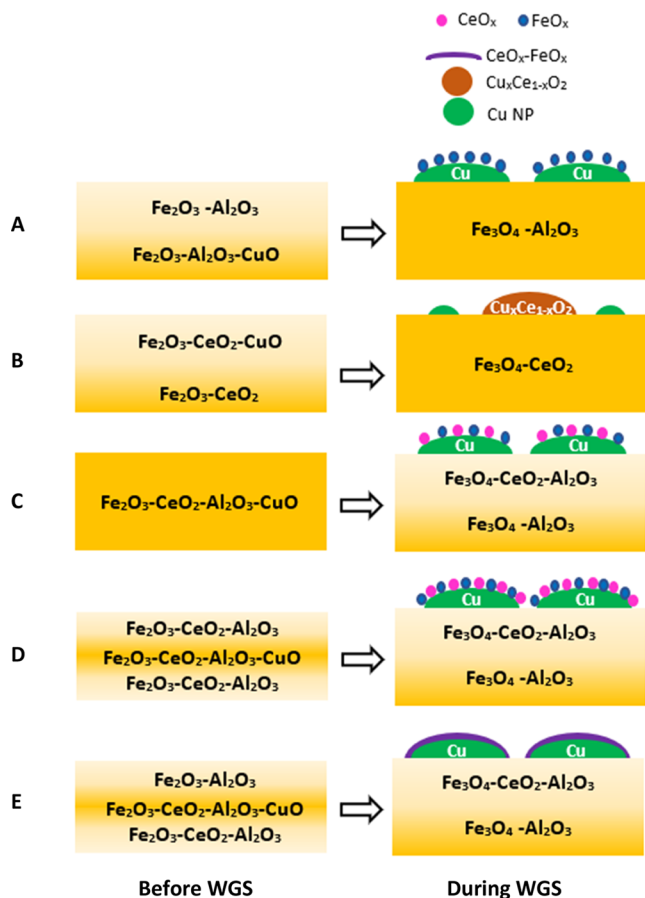**Figure 5.** Arrhenius plots for steady-state WGS reaction rates for Cu−Ce−Al−Fe oxide catalysts.

corresponding activation energy (E_a) values are listed in Table 2. The E_a values follow the trend: 3Cu8CeFe > 3Cu8AlFe ~ 3Cu5Al3CeFe > 3Ce/3Cu8AlFe ~ 5Ce/3Cu8AlFe. The general trend is that catalysts with higher E_a values correspond to lower TOF values.

4. DISCUSSION

4.1. Catalyst Structure. *4.1.1. Fresh Catalysts.* The freshly calcined catalysts possess the bulk Fe_2O_3 (hematite) phase (XRD and Raman), which is in agreement with previous literature reports.[47,57] The Al and Ce promoters form solid solutions with the Fe_2O_3 phase (shifts in the XRD and Raman band positions). Additional crystalline NPs of promoters are not observed (XRD and Raman). The Al is uniformly distributed between the outermost surface layer and subsurface region of the catalysts (HS-LEIS). Except for the 3Cu5Al3-CeFe catalyst, all of the other catalysts also exhibit uniform distributions of Ce between the outermost surface layer and subsurface region of the catalysts. For the 3Cu5Al3CeFe catalyst, the Ce is more concentrated in the subsurface region. In contrast, the Cu promoter is surface-enriched or segregated in all catalysts (HS-LEIS). A schematic of the initially calcined catalyst structures is shown in Scheme 1 (left).

4.1.2. RWGS-Activated Catalysts. Dynamic changes are observed after treatment of the catalysts with the RWGS reaction mixture. The bulk Fe_2O_3 phase of iron oxide transforms to the bulk Fe_3O_4 phase (XRD and Raman). This bulk phase transformation is associated with a significant decrease in the catalyst surface area (Table 1). Except for the 3Cu8CeFe catalyst, the other catalysts do not exhibit any crystal phase other than Fe_3O_4 (XRD and Raman). The Al is still uniformly distributed between the outermost surface layer and subsurface region of the catalysts after the RWGS treatment, whereas Ce surface-segregated (HS-LEIS). The Cu has been shown to form metallic Cu^0 NPs on the catalyst surface during the WGS reaction.[10] With the exception of the 3Cu8CeFe catalyst, the metallic Cu^0 NPs are decorated by secondary metal oxides (HS-LEIS). For the 3Cu8CeFe catalyst, the formation of the Ce−Cu−O mixed oxide phase is observed after the RWGS treatment (*in situ* Raman). Furthermore, it is observed that the Ce−Cu−O phase is present near the surface region of the catalyst (HS-LEIS), but it is not uniformly distributed (*in situ* Raman). A schematic of the activated catalyst structures is shown in Scheme 1 (right).

4.2. Structural Promotion. The uniform distribution of Al in the surface region, as opposed to surface segregation of Ce after the RWGS treatment (compare 3Cu8AlFe and 3Cu8CeFe catalysts in Figure 3), results in higher thermo-stability (Table 1). The Al promotion is also apparent in other Cu−Al−Ce−Fe catalysts (uniform Al distribution, Figure 3), exhibiting a higher surface area than the 3Cu8CeFe catalyst without Al promotion. Furthermore, the thermostability is even greater (lower decrease in surface area, Table 1) when Ce is added via impregnation of the precalcined 3Cu8AlFe catalyst, as opposed to coprecipitation in the 3Cu5Al3CeFe catalyst. These observations indicate that Al acts as a better structural promoter than Ce.

4.3. Functional Promotion. The Al is distributed uniformly throughout the surface and subsurface regions of the iron oxide-based catalysts after activation with the RWGS treatment (HS-LEIS) and, consequently, does not promote the catalytic active sites (FeO_x−Cu interfacial sites). In contrast, Ce is surface-segregated after RWGS treatment (HS-LEIS). Surface segregation is enhanced for the Ce-impregnated catalysts, where a higher ceria loading results in a thicker overlayer formation on the Cu NPs (compare Cu HS-LEIS signals in RWGS-treated 3Ce/3Cu8AlFe and 5Ce/3Cu8AlFe catalysts). This observation suggests that some CeO_x is most probably also decorating the surface of the Cu NPs forming a CeO_x−FeO_x−Cu interface. Thus, CeO_x serves as a functional promoter that is better than AlO_x.

4.4. Catalyst Structure−Activity Relationships and Role of Promoters. *4.4.1. 3Cu8AlFe Catalyst.* The Al promoter provides good structural stability, and the Cu−FeO_x interface provides very good functional promotion, resulting in moderate E_a and SS activity.

4.4.2. 3Cu8CeFe Catalyst. In the absence of the Al promoter, the catalyst exhibits poorer thermostability and the presence of the Ce−Cu−O mixed oxide phase hinders the formation of a highly active Cu−Fe_3O_4 interfacial sites.[10,19] Hence, despite possessing the highest number of the reducible active sites, the catalyst exhibits the highest E_a, low SS activity, and lowest TOF.

4.4.3. 3Cu5Al3CeFe Catalyst. The combination of Al with Ce promoters provides good structural stability, and the absence of the Ce−Cu−O mixed oxide phase allows for the formation of the CeO_x−FeO_x−Cu interfacial sites. The thick oxide overlayer on the Cu NPs, however, results in only minor

Scheme 1. Structures of (A) 3Cu8AlFe, (B) 3Cu8CeFe, (C) 3Ce/3Cu8AlFe, (D) 5Ce/3Cu8AlFe, and (E) 3Cu5Al3CeFe Catalysts before (Left) and during (Right) the WGS Reaction

improvement in SS activity and similar TOF and activation energy values.

4.4.4. 3Ce/3Cu8AlFe Catalyst. The Al provides excellent thermostability, and impregnation of a small amount of the Ce promoter results in a greater amount of the CeO_x−FeO_x−Cu interfacial sites. This results in the lowest E_a and the highest catalytic activity. This catalyst shows the synergistic effect of Ce and Al promotion toward the WGS/RWGS reaction.

4.4.5. 5Ce/3Cu8AlFe Catalyst. The higher loading of the Ce promoter results in a slightly thicker CeO_x overlayer on the Cu NPs (lower number of active sites) compared to the 3Ce/3Cu8AlFe catalyst. Overall, low E_a, very good catalytic activity, and higher TOF are observed.

5. CONCLUSIONS

Several Cr-free copper−iron oxide-based high-temperature water−gas shift catalysts were prepared with the Al promoter (3Cu8AlFe), Ce promoter (3Cu8CeFe), and copresence of both promoters (3Cu5Al3CeFe, 3Ce/3Cu8AlFe, and 5Ce/3Cu8AlFe). The 3Cu8CeFe catalyst exhibits the additional presence of a Ce−Cu−O mixed oxide phase in the RWGS-treated sample that was not detected from the Cu−Ce−Al−Fe oxide catalysts due to low ceria loading.

The Al promoter uniformly distributes through the outermost surface layer and subsurface layers of the catalyst and serves as a structural promoter that provides improved catalyst thermostability. The Ce promoter is surface-segregated and appears to decorate the Cu NPs to form a CeO_x−FeO_x−Cu interfacial area. The copresence of the Al and Ce promoters results in higher catalytic activity than the corresponding individual promotion because of the presence of a highly active Ce−Cu−Fe oxide interface. The impregnation of Ce onto the 3Cu8AlFe catalyst, as opposed to coprecipitation, results in the formation of a CeO_x overlayer on the Cu NPs with a higher Cu−CeO_x interfacial area leading to ∼50% increase in catalytic activity. The molecular level understanding from this study can guide the rational design of Cr-free HT-WGS catalysts.

■ AUTHOR INFORMATION

Corresponding Author

Israel E. Wachs − *Operando Molecular Spectroscopy & Catalysis Laboratory, Department of Chemical and Biomolecular Engineering, Lehigh University, Bethlehem, Pennsylvania 18015, United States;* ○ orcid.org/0000-0001-5282-128X; Email: iew0@lehigh.edu

Authors

Ozgen Yalcin − *College of Engineering and Technology, American University of the Middle East, Egaila 54200, Kuwait;* ○ orcid.org/0000-0003-2580-0832

Sagar Sourav − *Operando Molecular Spectroscopy & Catalysis Laboratory, Department of Chemical and Biomolecular Engineering, Lehigh University, Bethlehem, Pennsylvania 18015, United States;* ○ orcid.org/0000-0001-5892-1329

Complete contact information is available at:
https://pubs.acs.org/10.1021/acscatal.3c02474

Author Contributions

O.Y.: writing—original draft, conceptualization, investigation; S.S.: writing—review and editing; I.E.W.: funding acquisition, supervision, writing—review and editing.

Notes

The authors declare no competing financial interest.

■ ACKNOWLEDGMENTS

■ REFERENCES

(1) Smith R J, B.; Loganathan, M.; Shantha, M. S. A Review of the Water Gas Shift Reaction Kinetics. *Int. J. Chem. React. Eng.* **2010**, *8* (1), 1−32.

(2) Gradisher, L.; Dutcher, B.; Fan, M. Catalytic Hydrogen Production from Fossil Fuels via the Water Gas Shift Reaction. *Appl. Energy* **2015**, *139*, 335−349.

(3) Levalley, T. L.; Richard, A. R.; Fan, M. The Progress in Water Gas Shift and Steam Reforming Hydrogen Production Technologies - A Review. *Int. J. Hydrogen Energy* **2014**, *39* (30), 16983−17000.

(4) Ladebeck, J. R.; Wagner, J. P. Catalyst Development for Water-Gas Shift. In *Handbook of Fuel Cells*; John Wiley & Sons, Inc., 2003; Vol. 3, pp 190−201.

(5) Ratnasamy, C.; Wagner, J. P. Water Gas Shift Catalysis. *Catal. Rev.* **2009**, *51* (3), 325−440.

(6) Mendes, D.; Mendes, A.; Madeira, L. M.; Iulianelli, A.; Sousa, J. M.; Basile, A. The Water-Gas Shift Reaction: From Conventional Catalytic Systems to Pd-Based Membrane Reactors - a Review. *Asia-Pac. J. Chem. Eng.* **2010**, *5*, 111−137.

(7) Rhodes, C.; Hutchings, G. J.; Ward, A. M. Water-Gas Shift Reaction: Finding the Mechanistic Boundary. *Catal. Today* **1995**, *23* (1), 43−58.

(8) Lee, D. W.; Lee, M. S.; Lee, J. Y.; Kim, S.; Eom, H. J.; Moon, D. J.; Lee, K. Y. The Review of Cr-Free Fe-Based Catalysts for High-Temperature Water-Gas Shift Reactions. *Catal. Today* **2013**, *210*, 2−9.

(9) Keturakis, C. J.; Zhu, M.; Gibson, E. K.; Daturi, M.; Tao, F.; Frenkel, A. I.; Wachs, I. E. Dynamics of CrO_3-Fe_2O_3 Catalysts during the High-Temperature Water-Gas Shift Reaction: Molecular Structures and Reactivity. *ACS Catal.* **2016**, *6* (7), 4786−4798.

(10) Zhu, M.; Rocha, T. C. R.; Lunkenbein, T.; Knop-Gericke, A.; Schlogl, R.; Wachs, I. E. Promotion Mechanisms of Iron Oxide-Based High Temperature Water-Gas Shift Catalysts by Chromium and Copper. *ACS Catal.* **2016**, *6* (7), 4455−4464.

(11) Edwards, M. A.; Whittle, D. M.; Rhodes, C.; Ward, A. M.; Rohan, D.; Shannon, M. D.; Hutchings, G. J.; Kiely, C. J. Microstructural Studies of the Copper Promoted Iron Oxide/Chromia Water-Gas Shift Catalyst. *Phys. Chem. Chem. Phys.* **2002**, *4* (15), 3902−3908.

(12) Scariot, M.; Francisco, M. S. P.; Jordão, M. H.; Zanchet, D.; Logli, M. A.; Vicentini, V. P. An Investigation of the Activation Process of High Temperature Shift Catalyst. *Catal. Today* **2008**, *133−135* (1−4), 174−180.

(13) Patlolla, A.; Carino, E. V.; Ehrlich, S. N.; Stavitski, E.; Frenkel, A. I. Application of Operando XAS, XRD, and Raman Spectroscopy for Phase Speciation in Water Gas Shift Reaction Catalysts. *ACS Catal.* **2012**, *2* (11), 2216−2223.

(14) Zhu, M.; Wachs, I. E. Iron-Based Catalysts for the High-Temperature Water-Gas Shift (HT-WGS) Reaction: A Review. *ACS Catal.* **2016**, *6* (2), 722−732.

(15) Araujo, G. C.; Rangel, M. C.An Environmental Friendly Catalyst for the High Temperature Shift Reaction. In *Studies in Surface Science and Catalysis*; Elsevier, 2000; Vol. 130, pp 1601−1606.

(16) Martos, C.; Dufour, J.; Ruiz, A. Synthesis of Fe_3O_4-Based Catalysts for the High-Temperature Water Gas Shift Reaction. *Int. J. Hydrogen Energy* **2009**, *34* (10), 4475−4481.

(17) Gawade, P.; Mirkelamoglu, B.; Tan, B.; Ozkan, U. S. Cr-Free Fe-Based Water-Gas Shift Catalysts Prepared through Propylene

Oxide-Assisted Sol-Gel Technique. *J. Mol. Catal. A: Chem.* **2010**, *321* (1−2), 61−70.

(18) Zhang, L.; Wang, X.; Millet, J. M. M.; Matter, P. H.; Ozkan, U. S. Investigation of Highly Active Fe-Al-Cu Catalysts for Water-Gas Shift Reaction. *Appl. Catal., A* **2008**, *351* (1), 1−8.

(19) Zhu, M.; Yalçın, Ö.; Wachs, I. E. Revealing Structure-Activity Relationships in Chromium Free High Temperature Shift Catalysts Promoted by Earth Abundant Elements. *Appl. Catal., B* **2018**, *232*, 205−212.

(20) Sourav, S.; Wachs, I. E. Cr-Free, Cu Promoted Fe Oxide-Based Catalysts for High-Temperature Water-Gas Shift (HT-WGS) Reaction. *Catalysts* **2020**, *10* (3), No. 305.

(21) de Araújo, G. C.; do Rangel, M. C. An Environmental Friendly Dopant for the High-Temperature Shift Catalysts. *Catal. Today* **2000**, *62* (2−3), 201−207.

(22) Natesakhawat, S.; Wang, X.; Zhang, L.; Ozkan, U. S. Development of Chromium-Free Iron-Based Catalysts for High-Temperature Water-Gas Shift Reaction. *J. Mol. Catal. A: Chem.* **2006**, *260* (1−2), 82−94.

(23) Lee, J. Y.; Lee, D.-W.; Lee, K.-Y.; Wang, Y. Cr-Free Fe-Based Metal Oxide Catalysts for High Temperature Water Gas Shift Reaction of Fuel Processor Using LPG. *Catal. Today* **2009**, *146* (1−2), 260−264.

(24) Wang, H.; Wang, G.; Wang, X.; Bai, J. Hydrogen Production by Redox of Cation-Modified Iron Oxide. *J. Phys. Chem. C* **2008**, *112* (14), 5679−5688.

(25) Tabakova, T.; Manzoli, M.; Paneva, D.; Boccuzzi, F.; Idakiev, V.; Mitov, I. CO-Free Hydrogen Production over Au/CeO$_2$-Fe$_2$O$_3$ Catalysts: Part 2. Impact of the Support Composition on the Performance in the Water-Gas Shift Reaction. *Appl. Catal., B* **2011**, *101* (3−4), 266−274.

(26) Zhang, F.; Zheng, Q.; Wei, K.; Lin, X.; Zhang, H.; Li, J.; Cao, Y. Improved Performance of Au/Fe$_2$O$_3$ Catalysts Promoted with ZrO$_2$ and Nb$_2$O$_5$ in the WGS Reaction under Hydrogen-Rich Conditions. *Catal. Lett.* **2006**, *108* (3−4), 131−136.

(27) Meshkani, F.; Rezaei, M. High Temperature Water Gas Shift Reaction over Promoted Iron Based Catalysts Prepared by Pyrolysis Method. *Int. J. Hydrogen Energy* **2014**, *39* (29), 16318−16328.

(28) Bouarab, R.; Bennici, S.; Mirodatos, C.; Auroux, A. Hydrogen Production from the Water-Gas Shift Reaction on Iron Oxide Catalysts. *J. Catal.* **2014**, *2014*, 1−6.

(29) Kappen, P.; Grunwaldt, J. D.; Hammershoi, B. S.; Troger, L.; Clausen, B. S. The State of Cu Promoter Atoms in High-Temperature Shift Catalysts - An in Situ Fluorescence XAFS Study. *J. Catal.* **2001**, *198* (1), 56−65.

(30) Puig-Molina, A.; Cano, F. M.; Janssens, T. V. W. The Cu Promoter in an Iron-Chromium-Oxide Based Water-Gas Shift Catalyst under Industrial Conditions Studied by in-Situ XAFS. *J. Phys. Chem. C* **2010**, *114* (36), 15410−15416.

(31) Estrella, M.; Barrio, L.; Zhou, G.; Wang, X.; Wang, Q.; Wen, W.; Hanson, J. C.; Frenkel, A. I.; Rodriguez, J. A. In Situ Characterization of CuFe$_2$O$_4$ and Cu/Fe$_3$O$_4$ Water - Gas Shift Catalysts. *J. Phys. Chem. C* **2009**, *113*, 14411−14417.

(32) Zhu, M.; Wachs, I. E. Determining Number of Active Sites and TOF for the High-Temperature Water Gas Shift Reaction by Iron Oxide-Based Catalysts. *ACS Catal.* **2016**, *6* (3), 1764−1767.

(33) Ladebeck, J.; Kochloefl, K. Cr-Free Iron-Catalysts for Water-Gas Shift Reaction. In *Studies in Surface Science and Catalysis*; Elsevier, 1995; Vol. *91*, pp 1079−1083.

(34) Na, H.-S.; Jeong, D.-W.; Jang, W.-J.; Shim, J.-O.; Roh, H.-S. The Effect of Preparation Method on Fe/Al/Cu Oxide-Based Catalyst Performance for High Temperature Water Gas Shift Reaction Using Simulated Waste-Derived Synthesis Gas. *Int. J. Hydrogen Energy* **2015**, *40* (36), 12268−12274.

(35) Liu, Q.; Ma, W.; He, R.; Mu, Z. Reaction and Characterization Studies of an Industrial Cr-Free Iron-Based Catalyst for High-Temperature Water Gas Shift Reaction. *Catal. Today* **2005**, *106* (1−4), 52−56.

(36) Meshkani, F.; Rezaei, M. High-Temperature Water-Gas Shift Reaction over Nanostructured Cr-Free Fe$_2$O$_3$-Al$_2$O$_3$-CuO-MO (M: Ba, Ca, Mg and Sr) Catalysts for Hydrogen Production. *J. Ind. Eng. Chem.* **2015**, *30*, 353−358.

(37) Jeong, D.-W.; Subramanian, V.; Shim, J.-O.; Jang, W.-J.; Seo, Y.-C.; Roh, H.-S.; Gu, J. H.; Lim, Y. T. High-Temperature Water Gas Shift Reaction Over Fe/Al/Cu Oxide Based Catalysts Using Simulated Waste-Derived Synthesis Gas. *Catal. Lett.* **2013**, *143*, 438−444.

(38) Meshkani, F.; Rezaei, M. Promoted Fe$_2$O$_3$-Al$_2$O$_3$-CuO Chromium-Free Catalysts for High-Temperature Water-Gas Shift Reaction. *Chem. Eng. Technol.* **2015**, *38* (8), 1380−1386.

(39) Yamaguchi, D.; Tang, L.; Burke, N.; Trimm, D.; Chiang, K.; Nguyen, K. In *Redox Performance of Modified Iron Oxides for Hydrogen Production*, Novel Gas Conversion Symposium 9; Elsevier: Lyon, France, 2011.

(40) Ou, X.-J.; Cheng, J.-Y.; Wang, H.-M.; Xiao, Y. Effects of Metal Oxides on Stability and Activity of Iron-Based Chromia-Free Catalysts for Water-Gas Shift Reaction. *J. Nat. Gas Chem.* **1999**, 231−237.

(41) Reddy, G. K.; Boolchand, P.; Smirniotis, P. G. Unexpected Behavior of Copper in Modified Ferrites during High Temperature WGS Reaction-Aspects of Fe^{3+}↔Fe^{2+} Redox Chemistry from Mossbauer and XPS Studies. *J. Phys. Chem. C* **2012**, *116* (20), 11019−11031.

(42) Reddy, G. K.; Smirniotis, P. G. Effect of Copper as a Dopant on the Water Gas Shift Activity of Fe/Ce and Fe/Cr Modified Ferrites. *Catal. Lett.* **2011**, *141* (1), 27−32.

(43) Reddy, G. K.; Gunasekara, K.; Boolchand, P.; Smirniotis, P. G. Cr- and Ce-Doped Ferrite Catalysts for the High Temperature Water-Gas Shift Reaction: TPR and Mossbauer Spectroscopic Study. *J. Phys. Chem. C* **2011**, *115* (4), 920−930.

(44) Trovarelli, A.; de Leitenburg, C.; Dolcetti, G. Design Better Cerium-Based Oxidation Catalysts. *Chemtech* **1997**, *27*, 32−37.

(45) Phivilay, S. P.; Puretzky, A. A.; Domen, K.; Wachs, I. E. Nature of Catalytic Active Sites Present on the Surface of Advanced Bulk Tantalum Mixed Oxide Photocatalysts. *ACS Catal.* **2013**, *3* (12), 2920−2929.

(46) Zhu, M.; Chen, J.; Shen, L.; Ford, M. E.; Gao, J.; Xu, J.; Wachs, I. E.; Han, Y. Probing the Surface of Promoted CuO-Cr$_2$O$_3$-Fe$_2$O$_3$ Catalysts during CO$_2$ Activation. *Appl. Catal., B* **2020**, *271*, No. 118943.

(47) Morris, M. C.; McMurdie, H. F.; Evans, E. H.; Paretzkin, B.; Parker, H. S.; Panagiotopoulos, N. C.; Hubbard, C. R. *Standard X-Ray Diffraction Powder Patterns : Section 18- Data for 58 Substances*; National Bureau of Standards: Gaithersburg, MD, 1981, p 37.

(48) Cava, S.; Tebcherani, S. M.; Souza, I. A.; Pianaro, S. A.; Paskocimas, C. A.; Longo, E.; Varela, J. A. Structural Characterization of Phase Transition of Al$_2$O$_3$ Nanopowders Obtained by Polymeric Precursor Method. *Mater. Chem. Phys.* **2007**, *103* (2−3), 394−399.

(49) Sudarsanam, P.; Mallesham, B.; Durgasri, D. N.; Reddy, B. M. Physicochemical Characterization and Catalytic CO Oxidation Performance of Nanocrystalline Ce-Fe Mixed Oxides. *RSC Adv.* **2014**, *4* (22), 11322−11330.

(50) Shannon, R. D. Revised Effective Ionic Radii and Systematic Studies of Interatomic Distances in Halides and Chalcogenides. *Acta Crystallogr., Sect. A* **1976**, *32* (5), 751−767.

(51) Cornell, R. M.; Schwertmann, U. *The Iron Oxides: Structure, Properties, Reactions, Occurences and Uses*; WILEY-VCH Verlag GmbH & Co. KGaA: Weinheim, 2003; p 147.

(52) Perez-Alonso, F. J.; López Granados, M.; Ojeda, M.; Herranz, T.; Rojas, S.; Terreros, P.; Fierro, J. L. G.; Gracia, M.; Gancedo, J. R. Relevance in the Fischer−Tropsch Synthesis of the Formation of Fe-O-Ce Interactions on Iron-Cerium Mixed Oxide Systems. *J. Phys. Chem. B* **2006**, *110* (47), 23870−23880.

(53) Shebanova, O. N.; Lazor, P. Raman Spectroscopic Study of Magnetite (FeFe$_2$O$_4$): A New Assignment for the Vibrational Spectrum. *J. Solid State Chem.* **2003**, *174* (2), 424−430.

(54) Shan, W.; Shen, W.; Li, C. Structural Characteristics and Redox Behaviors of $Ce_{1-X}Cu_xO_y$ Solid Solutions. *Chem. Mater.* **2003**, *15* (25), 4761−4767.

(55) Anantharaman, M. R.; Reijne, S.; Jacobs, J. P.; Brongersma, H. H.; Smits, R. H. H.; Seshan, K. Preferential Exposure of Certain Crystallographic Planes on the Surface of Spinel Ferrites: A Study by LEIS on Polycrystalline Spinel Ferrite Surfaces. *J. Mater. Sci.* **1999**, *34*, 4279−4283.

(56) de Ridder, M.; van de Ven, P. C.; van Welzenis, R. G.; Brongersma, H. H.; Helfensteyn, S.; Creemers, C.; Van Der Voort, P.; Baltes, M.; Mathieu, M.; Vansant, E. F. Growth of Iron Oxide on Yttria-Stabilized Zirconia by Atomic Layer Deposition. *J. Phys. Chem. B* **2002**, *106*, 13146−13153.

(57) Lyubutin, I. S.; Lin, C. R.; Korzhetskiy, Y. V.; Dmitrieva, T. V.; Chiang, R. K. Mössbauer Spectroscopy and Magnetic Properties of Hematite/Magnetite Nanocomposites. *J. Appl. Phys.* **2009**, *106*, No. 034311, DOI: 10.1063/1.3194316.